First-principles Studies of Surfaces of a Metallic Oxide: ReO_3

A Thesis

Submitted in partial fulfillment for the Degree of

MASTER OF SCIENCE

as a part of Integrated Ph.D. programme in

MATERIALS SCIENCE

by

Suchitra

CHEMISTRY AND PHYSICS OF MATERIALS UNIT
JAWAHARLAL NEHRU CENTRE FOR ADVANCED SCIENTIFIC RESEARCH
Bangalore – 560 064

APRIL 2014

To my Family

DECLARATION

I hereby declare that the matter embodied in the thesis entitled "**First-principles Studies of Surfaces of a Metallic Oxide: ReO_3**" is the result of investigations carried out by me at the Chemistry and Physics of Materials Unit, Jawaharlal Nehru Centre for Advanced Scientific Research, Bangalore, India under the supervision of Prof. Umesh V. Waghmare and that it has not been submitted elsewhere for the award of any degree or diploma.

In keeping with the general practice in reporting scientific observations, due acknowledgement has been made whenever the work described is based on the findings of other investigators.

Suchitra

CERTIFICATE

I hereby certify that the matter embodied in this thesis entitled "**First-principles Studies of Surfaces of a Metallic Oxide: ReO_3**" has been carried out by Ms. Suchitra at the Chemistry and Physics of Materials Unit, Jawaharlal Nehru Centre for Advanced Scientific Research, Bangalore, India under my supervision and that it has not been submitted elsewhere for the award of any degree or diploma.

Prof. Umesh V. Waghmare
(Research Supervisor)

Acknowledgements

First of all, I would like to convey my gratitude to my advisor Prof. Umesh V. Waghmare for his constant guidance, encouragement and motivation. His enthusiasm for science has always motivated me. It is a rich and fulfilling experience to work under his guidance.

I am thankful to Prof. Balasubramanian Sundaram, Prof. Chandrabhas Narayana, Prof. Eswaramoorthy M., Prof. G.U. Kulkarni, Prof. K.S. Narayan, Dr. Kanishka Biswas, Dr. Rajesh Ganapathy, Dr. Ranjan Datta, Dr. Sebastian C Peter, Prof. Shivaprasad S. M., Prof. Shobhana Narasimhan, Prof. Subir K. Das, Prof. Sundaresan A., Prof. Umesh V. Waghmare, and Prof. Vidhyadhiraja N. S. for the courses they offered and wonderful classes which helped me in my research work.

I would like to thank specially Jayashree for suggestions and helping me in various possible ways.

I would like to thank my labmates Summaya, Sharmila, Meha, Koushik, Arpita, Anjali, KM and Pawan for various important discussions. I have learnt a lot from them.

I am thankful to my Integrated Ph.D. batchmates Abhijeet, Dipanwita, Rajib, Raaghesh, Sonu and Uttam for all the fun we had together in JNCASR. I would like to thank Uttam for being a great support and wonderful friend. I am also grateful to Ph.D. and Intrgrated Ph.D. seniors for all their help during initial days of JNCASR.

I would like to thank our Lab Convenors. I am also thankful to Mr. Ala Srinivas Rao who helped us in solving various experimental problems we had during our

practicals.

I am thankful to the present and past chairman of our department, Prof. S. Balasubramanian and Prof. G. U. Kulkarni for providing and maintaining various facilities to all the students.

I would also like to thank my school and college friends with whom i have spent some of the best time of my life.

I am grateful to the Thematic Unit of Excellence on Computational Materials Science (TUE-CMS) for providing the computational resources. Special thanks to Prof. Bala and Vijay.

Finally, I would like to thank my parents, brothers and sisters for their unending support, encouragement and showing faith in me.

Synopsis

With the theoretical and experimental advances, it has become possible to understand and control materials at different scales and time. In this thesis, we use density functional theory to study structure, electronic and vibrational properties of transition metal oxide surfaces. Transition metal oxides have a wide range of physical and chemical properties and are central to the emerging field of oxide electronics. However, they are greatly influenced by defects, particularly oxygen vacancies, which are always present in oxides. Surfaces of materials are known to show interesting properties which is absent in its bulk form. In this thesis, we have shown the effect of terminations and concentration of oxygen vacancies on various properties of materials like work function, surface energy, electronic struture and structural relaxations. Metallic ReO_3 nanocrystal shows surface enhanced Raman scattering (SERS) upon adsorption of aza-aromatics compound. In the second part of thesis we have shown that both electromagnetic and chemical enhancements are responsile for the experimentally observed phenomena. We have highlighted the orientaion of molecule on the surface and the interaction of molecule with surface.

List of Figures

List of Tables

Contents

Chapter 1

Introduction

Transition metal oxides exhibit a wide range of behavior ranging from metallic conductivity, insulating, superconducting, ferroelectricity, colossal magnetoresistance, etc. They have applications ranging from catalysis, solar cells to electronic devices. Recently, a lot of interesting phenomena have been discovered at the interfaces of oxide heterostructures. Electron gas at the interface of two insulators [2], coexistence of superconductivity and magnetism [3], improper ferroelectricity at the interface of ferroelectric and paraelectric superlattice [4], etc. Also, the surfaces of TMO have been well studied both experimentally and theoretically [5]. The presence of a surface leads to breaking of translational symmetry. Atoms at the surface adjust to the breaking of symmetry by surface reconstruction, surface rumpling, and local polyhedral rearrangement. All these processes at the surface, the presence of dangling bonds and, low coordination number of atoms at the surface lead to new properties of a surface which may not be present in the bulk form. For example, at the surface of superconducting Sr_2RuO_4, the lattice distortion involving octahedral rotations couples with spin fluctuations leading to stable ferromagnetic state at the surface [6]. $SrTiO_3$ exhibits local polar distortion due to rearrangements in

the surface atomic planes [7] which are absent in the bulk. The in-plane MO_6 octahedral rotations of opposite sense in adjacent unit cells of a perovskite oxide lead to antiferrodistortive (AFD) ordering at $PbTiO_3$ surface which is otherwise absent in the bulk [8]. In other words, novel properties can emerge at the interface between two different materials or through creation of surface of such oxides. Wide variety of properties of TMO may open the gate for multifunctional devices of the future. Unlike semiconductors it has more knobs than just voltage, more responses than just density or current; rich electronic behavior and more functionalities than just bi-state of current. With advances in experimental techniques like pulse laser deposition, molecular beam epitaxy, it is now possible to grow films with precision of atomic plane; and construct interfaces and surfaces with desired atomic terminations [9]. Through theoretical advances it has now become possible to understand the behavior of surfaces and interfaces.

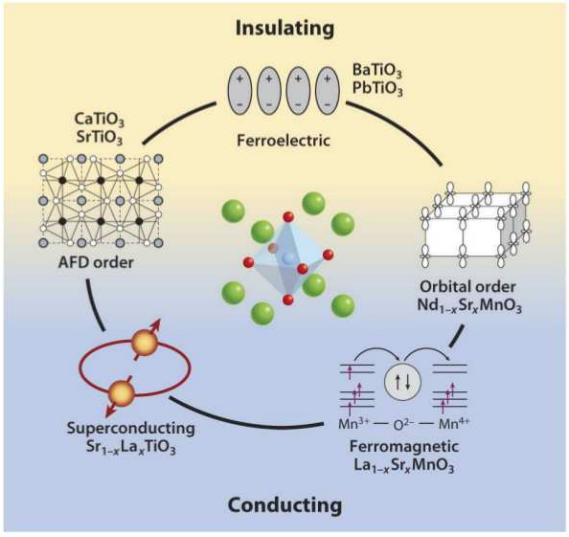

Figure 1.1: Schematic representation of properties and phenomena exhibited by the transition metal oxides. Ref. [1]

TMO often contain point defects, particularly oxygen vacancies, which can significantly alter their magnetic, electronic, orbital and transport properties due to changes in the oxidation state. The oxygen vacancies acts as a source of electrons,

the exchange interaction between electron spins leads to the development of ferromagnetism at nanocrystal surface of non-magnetic or diamagnetic oxides [10]. The oxygen vacancies induces strain (between 1 to 10%) particularly chemical expansivity in the system [11]. Tensile strain greater than 1% can lead to change in the magnetic susceptibilities and in the orderings of spins. Oxides grown on substrate with large lattice constant undergo tensile strain; this strain is minimized if oxygen vacancies' volume is greater than the lattice oxygen [12]. This also suggest the growth of heterostructures with large lattice mismatch. The presence of oxygen vacancies lead to decrease in the work function with vacancies concentration due to reduction in the cation oxidation state [13]. Adsorption at the surface also affect the work function.

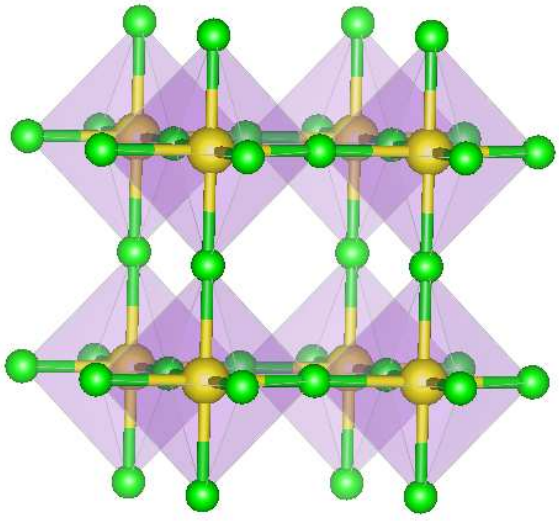

Figure 1.2: Crystal structure of ReO_3.

TMO can be a simple type binary or a ternary type with a complex crystal structures. Among them rhenium trioxide (ReO_3) is a binary transition metal oxide with a high symmetric cubic structure and Re coordinated octahedrally to O atoms (Fig. 1.2). Its structure remain undistorted even at high temperatures. Razavi and co-workers [14] observed some anamoly in Fermi surface under pressure and discovered the phase transitions of ReO_3 under pressure. It is conducting in nature,

and its electrical conductivity is surprisingly comparable to that of copper. Its nanocrystal shows enhancement in Raman signal called Surface Enhanced Raman Scattering (SERS), for example in the adsorption of pyridine. SERS is the result of electromagnetic enhancement (EM) and chemical enhancement (CM). EM is a long range and dominant effect involving amplification of electric field near molecule due to coupling of electromagnetic radiation with surface plasmon of metal nanocrystals. CM is short range and weak effect arising due to interaction between adsorbate and molecule [15]. The thesis is basically focussed on the investigation of structure, electronic and vibrational properties of (001) surfaces of ReO_3. We have investigated the possible reason for SERS by adsorbing pyridine on the most stable surface. We have used first-principles calculations based on the density functional theroy (DFT) to determine these properties.

We organize the rest of thesis as follows: In **chapter 2** we present methods and formalism used in our calculations. This chapter covers the theoretical aspects of density functional theory (DFT) and density functional perturbation theroy (DFPT). We highlight various approximations and limitations of these theoretical techniques in this chapter.

Properties of TMOs are greatly influenced by defects, particularly the oxygen vacancies which are always present in experimental samples. In **Chapter 3**, we show that by controlling oxygen vacancies at the (001) surface of ReO_3, its work function can be tuned from 7 to 3 eV. The work function is shown to correlate directly with the stability of surface, with linear dependence on surface energy. We further assess the stability of ReO_3 surface by determining its phonon dispersion, and explain how the stresses developed at the surface effectively may lead to size dependence of its pressure dependent structural phase transitions observed experimentally.

Metal surfaces like Ag, Au and Cu have been known to show enhancement in the Raman signal, called Surface Enhanced Raman Scattering (SERS) of a molecule.

ReO_3 nanocrystal, being a metal oxide, interestingly shows enhancement in the range of 10^5 -10^6 after adsorption of pyridine. In **Chapter 4**, we have shown that pyridine adsorbs through quite a strong bonding with the surface, and there is a strong electric field near molecule. Our calculations predict that both electromagnetic and chemical enhancements are responsible for SERS observed experimentally. Through calculations of phonons, we provide a reason for red-shift and blue shift in frequencies observed in Raman spectra experimentally. Finally, we conclude and summarize our results in **Chapter 5**.

Chapter 2

Methods

2.1 Density Functional Theory

2.1.1 Introduction

With advances in quantum mechanics, it is well established that various properties of a material can be explained by behavior of electrons in the presence of other electrons, nuclei or other perturbation. The Hamiltonian of a system which takes into account electron-electron, electron-nuclear and nuclear-nuclear interactions is given by:

$$\hat{H} = -\frac{\hbar^2}{2m_e}\sum_i \nabla_i^2 - \sum_{i,I}\frac{Z_i e^2}{|\mathbf{r}_i - \mathbf{R}_I|} + \frac{1}{2}\sum_{i\neq j}\frac{e^2}{|\mathbf{r}_i - \mathbf{r}_j|} - \sum_I \frac{\hbar^2}{2M_I}\nabla_I^2 + \frac{1}{2}\sum_{I\neq J}\frac{Z_I Z_J e^2}{|\mathbf{R}_I - \mathbf{R}_J|} \tag{2.1}$$

where electrons are denoted by lowercase subscripts and nuclei, with charge Z_I and mass M_I, denoted by uppercase subscripts. The first term in Equation 2.1 is the kinetic energy of electrons, the second term represents the interaction between electrons and nuclei (termed as external potential), the third term is the interaction between electrons, the fourth term is the kinetic energy of nuclei and the fifth term

is the interaction between nuclei. The mass of nucleus is approximately >1836 times larger than that of an electron, and hence its kinetic energy can be neglected. This approximation is called as the **Born-Oppenheimer Approximation**. The Hamiltonian in Equation 2.1 will then reduce to:

$$\hat{H} = \hat{T} + \hat{V}_{ext} + \hat{V}_{int} + E_{II} \tag{2.2}$$

where $\hat{T}$ is the kinetic energy operator, $\hat{V}_{ext}$ is the potential acting on electrons due to nuclei, $\hat{V}_{int}$ is the electron-electron interaction and E_{II} is the classical interaction of nuclei with one another. The properties can be derived by solving the time-independent Schrödinger equation:

$$\hat{H}\Psi(\mathbf{R}, \mathbf{r}) = \varepsilon\mathbf{\Psi}(\mathbf{R}, \mathbf{r}) \tag{2.3}$$

$\mathrm{r} \equiv \{r_1, r_2, r_3, ..., r_N\}$ is the set of N electronic coordinates.

$\mathrm{R} \equiv \{R_1, R_2, R_3, ..., R_P\}$ is the set of P nuclear coordinates.

Where $\varepsilon' s$ are energy eigenvalues and $\Psi(\mathbf{R}, \mathbf{r})' s$ are the corresponding wavefunctions. Ψ is asymmetric with respect to exchange of electronic coordinates in $\mathbf{r}$ and asymmetric or symmetric with respect to exchange of nuclear variables in $\mathbf{R}$.

It is quite difficult to solve Schrödinger's Equation 2.3 accurately. Various approximations have been developed to solve it. Independent electron approximation is the oldest approximation which consider that interaction between the electrons can be ignored. Hartree approximation modified it further by treating the electrons as independent, but interacting only via the mean-field Coulomb potential. Hartree did not consider the asymmetric nature of electronic wavefunctions. Anti-symmetric nature of electrons was considered in the Hartree-Fock Approximation. In this framework, asymmetric electronic wavefunction can be written in the form

of a Slater determinant such that the wavefunctions are indistinguishable.

Density functional theory is another approach which treat many body system accurately, and is efficient to apply. It has excluded the problem of 3N-variables (N is the number of electrons and their associated 3 spatial variables) associated with many electron-wave function with a functional of electron density which reduces the number of variables to 3, and hence has reduces the complexity of many electron problem to a great extent. In other words, it allows one to map exactly the problem of strongly interacting electron gas onto that of a single particle moving in an effective potential arising from the rest.

2.1.2 Hohenberg-Kohn Theorems

Hohenberg and Kohn proposed that the ground state energy of the system uniquely depends on the electron density in their first theorem. They proved that the ground state energy can be obtained by minimizing the energy of system according to electron density. Their theorems can be stated as follows:

Theorem I: The external potential $V_{ext}(\mathbf{r})$ of an interacting particle system is uniquely determined by the ground state density $n_o(\mathbf{r})$, besides a constant.

Theorem II: The universal energy functional E[n] can be defined in terms of density $n_o(\mathbf{r})$ for any external potential $V_{ext}(\mathbf{r})$. The global minimum value of this functional is the ground state energy of the system for any $V_{ext}(\mathbf{r})$. The density $n_o(\mathbf{r})$ that minimizes it is the ground state density $n_o(\mathbf{r})$.

The properties like the kinetic energy, etc., can be determined uniquely if $n(\mathbf{r})$ is specified, then each such property can be viewed as a functional of $n(\mathbf{r})$, including

the total energy functional. The total energy functional can be given as:

$$E_{HK}[n] = F_{HK}[n] + \int d^3r V_{ext}(\mathbf{r})n(\mathbf{r}) + E_{II} \tag{2.4}$$

E_{II} is the interaction energy of nuclei. Functional $F_{HK}[n]$ includes all internal energies, kinetic energies and potential of interacting electron system and is given by:

$$F_{HK}[n] = T[n] + E_{int}[n] \tag{2.5}$$

$F_{HK}[n]$ is universal by construction since the kinetic energy and interaction energy of the particles are functionals only of the density.

In order to evaluate the kinetic energy exactly, the only known practical way is to revert to the usual expression in terms of set of N wavefunctions. There is no known explicit functional to go directly from the density to the kinetic energy. A more general approach was suggested by Kohn and Sham (1965). They included the kinetic energy of non-interacting electrons in terms of independent particle wavefunctions, in addition to interaction terms modelled as a functional of the density.

2.1.3 Kohn-Sham Ansatz

The ansatz of Kohn and Sham assumes that the ground state density of the original interacting system is equal to that of some chosen non-interacting system i.e, one can map an interacting problem into a non-interacting problem. This leads to an independent-particle equations for the non-interacting system that can be considered exactly soluble with all difficult many-body terms incorporated into an exchange-correlation functional of the density. The non-interacting system can be described by single-particle equations and the corresponding Slater determinant is the ground state solution.

Using Kohn-Sham approach the energy functional can now be written as:

$$E[n(\mathbf{r})] = T_s[n(\mathbf{r})] + \frac{1}{2}\int \frac{n(\mathbf{r})n(\mathbf{r}')d^3r d^3r'}{|\mathbf{r}-\mathbf{r}'|} + \int n(\mathbf{r})V_{ext}(\mathbf{r})dr + E_{xc}[n(\mathbf{r})] \quad (2.6)$$

The first term is the kinetic energy of electrons, the second term is the electrostatic interaction energy between electrons, the third term is the interaction energy of electrons with external potential and the fourth term is the exchange-correlation interaction between electrons.

Here, the electron density is constructed as:

$$n(\mathbf{r}) = \sum_i |\Psi_i(\mathbf{r})|^2 \quad (2.7)$$

Here i refers to single-particle states and the sum is over all the occupied states. $E_{xc}[n(\mathbf{r})]$ is called the exchange-correlation energy functional. Taking functional derivative $\delta E[n(\mathbf{r})]/\delta\Psi_i^*(\mathbf{r})$ with the constraint that each $\Psi_i(\mathbf{r})$ normalized to unit leads to:

$$\left(-\frac{\hbar^2}{2m}\nabla_I^2 + V_{KS}(\mathbf{r})\right)\Psi_i(\mathbf{r}) = \varepsilon_i\Psi_i(\mathbf{r}) \quad (2.8)$$

where, V_{KS} is the Kohn-Sham potential for the non-interacting system given as:

$$V_{KS}(\mathbf{r}) = V_{ext}(\mathbf{r}) + \int \frac{n(\mathbf{r}')}{|\mathbf{r}-\mathbf{r}'|}dr + V_{xc}[n(\mathbf{r})], \quad (2.9)$$

where the first term is the external potential, the second term is the Hartree potential. The last term is the exchange-correlation potential defined as:

$$V_{xc}[n(\mathbf{r})] = \frac{\delta E_{xc}[n(\mathbf{r})]}{\delta n(\mathbf{r})} \quad (2.10)$$

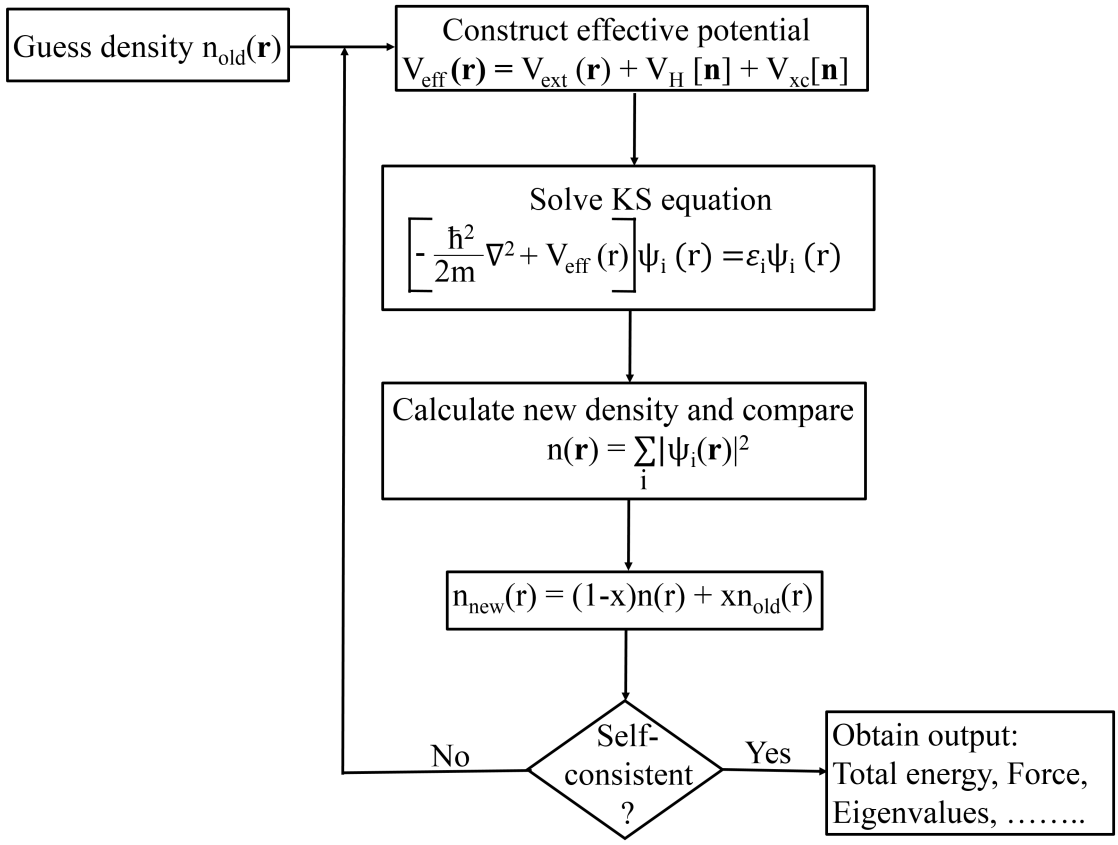

Figure 2.1: Self-consistency loop for the iterative solution of the KS equation.

2.1.4 Exchange-Correlation Energy Functional

Electrons are Fermions, hence the wavefunction of many electron system should be asymmetric under exchange of any two electrons. This produces a spatial separation between the electrons that have same spin leading to reduction in the Coulomb energy of electronic system. The reduction in energy due to antisymmetric nature of wavefunction is called the exchange energy, this is generally referred to as the Hartree-Fock approximation. The coulomb energy of the system is also reduced at the cost of increase in kinetic energy when the electrons of same spin are spatially separated. The difference between the many body energy of an electronic system and that calculated in the Hartree-Fock approximation is called the correlation energy. It is quite difficult to determine the exact value of exchange-correlation functional

due to electron-electron interactions involved. Kohn Sham replaces many electron problem by single electron equation. The exchange correlation energy functional Kohn Sham approach can be defined as:

$$E_{xc}[n(\mathbf{r})] = T[n(\mathbf{r})] - T_o[n(\mathbf{r})] + E_{ee}[(\mathbf{r})] - E_H[n(\mathbf{r})] \tag{2.11}$$

Here, $\mathrm{T}_o[n(\mathbf{r})]$ and $\mathrm{E}_{ee}[(\mathbf{r})]$ are exact kinetic and electron-electron interaction energies respectively. Since, exact value of E_{xc} is not known; so various approximations based on electron density have been introduced to describe it. Local density approximation (LDA) and the generalized gradient approximation (GGA) are the two approximations which are used to calculate the correlation energy. Here, we will discuss LDA only.

2.1.5 LDA

In this approximation, the exchange-correlation energy of an electronic system is constructed by assuming that the exchange-correlation energy per electron ($\varepsilon_{xc}(\mathbf{r})$) at a point $\mathbf{r}$ in the electron gas is equal to the exchange-correlation energy per electron of a homogenous electron gas that has the same density as the electron density at a point $\mathbf{r}$. Thus,

$$E_{xc}[n(\mathbf{r})] = \int \varepsilon_{xc}(\mathbf{r}) n(\mathbf{r}) d^3r \tag{2.12}$$

and

$$\frac{\delta E_{xc}[n(\mathbf{r})]}{\delta n(\mathbf{r})} = \frac{\partial [n(\mathbf{r})\varepsilon_{xc}(\mathbf{r})]}{\partial n(\mathbf{r})} \tag{2.13}$$

with

$$\varepsilon_{xc}(\mathbf{r}) = \varepsilon_{xc}^{hom}[n(\mathbf{r})] \tag{2.14}$$

The local density approximations assumes that the effects of exchange and correlations are local in character. The Perdew-Zunger (PZ), Perdew-Wang (PW), and Vosko-Wilk-Nusair (VWN) functionals are all common LDA functionals.

2.1.6 Basis Set

Numerical solution of Kohn Sham equations requires us to choose a mathematical representation for the one electron orbital i.e, we need a basis to expand the wave functions Ψ_n, and then truncate the basis (so that the calculation time is finite). Different types of basis sets are Plane-wave, atomic orbitals and mixed (set of atom centered basis set along with plane waves or other basis sets). For isolated systems such as atoms and molecules, atomic orbital basis is commonly used. For extended periodic systems, the system is represented by a basis set of mutually orthonormal basis.

For an extended system, the plane-wave basis set required to expand the electronic wave functions is often very large. Considering infinite system as a repeating array of unit cells allow us to expand finite number of electronic wave functions. Also, the potential experienced by an electron is invariant under crystal lattice translation i.e, $V_{ext}(\mathbf{r}) = V_{ext}(\mathbf{r+R})$ where, R is a lattice vector.

Bloch's theorem states that in periodic solid each electronic wave functions can be written as the product of a cell-periodic part and a wavelike part:

$$\psi_{jk}(\mathbf{r}) = u_{jk}(\mathbf{r})e^{i\mathbf{k}.\mathbf{r}}. \tag{2.15}$$

Here, u_{jk} is a cell periodic part, and exponential term is a plane wave. The cell-periodic part can be extended as a discrete set of plane waves whose wave vectors are reciprocal lattice vectors ($\mathbf{G}$) of the crystal.

$$u_{jk} = \sum_{G} C_{jk}(\mathbf{G}) e^{i\mathbf{G}.\mathbf{r}}. \tag{2.16}$$

Therefore, each electronic wave function can be written as a sum of plane waves,

$$\psi_{jk} = \sum_{G} C_{j,k+G} e^{[i(\mathbf{k}+\mathbf{G}).\mathbf{r}]} \tag{2.17}$$

For non-periodic systems like surfaces, some vacuum is added to the repeating crystal slab such that faces of crystal donot interact with each other. Isolated molecules can be also studied in similar fashion, keeping molecule in a box such that the interaction between molecules is negligible.

The kinetic energy of plane waves is given by the following relations:

$$T_{|k+G|} = \frac{\hbar^2 |\mathbf{k}+\mathbf{G}|^2}{2m} \tag{2.18}$$

The plane waves basis with smaller kinetic energy are more important than those with larger kinetic energy. So, plane waves are truncated by using an energy cutoff parameter E_{cut}.

The advantage of plane wave basis is that they are independent of atomic positions, and they represent all region of space with the same resolution. So, Hellmann-Feynmann theorem can be used readily to evaluate forces. The calculation of energy and its derivative is analytic and quite simple. Also, the quality of the basis is controlled by a single parameter. The main shortcoming of plane wave basis comes from the fact that the valence wavefunctions oscillate rapidly in the region occupied by the core electrons due to the strong ionic potential in this region. This

demands a large basis set, making it computationally expensive. Pseudopotential approximation discussed in the following section is the solution to this problem.

2.1.7 Pseudopotential approximation

In solids or molecules the core electrons are tightly bound to the nucleus and donot take part in bonding. So, core electrons are removed from the calculation, and the interaction of the valence electrons with the nucleus plus the core states is replaced by an effective screened potential. This is termed as a pseudopotential approximation. The solution of the atomic Schrödinger's equation for the pseudopotential is a pseudo-wave function different from the true wave function. The pseudopotential is constructed in such a way that its scattering properties are similar to those of the all-electron potential. It requires less number of basis functions and hence is computationally efficient, without compromising much on the properties of system.

Pseudopotentials are constructed using a cutoff radius (r_c) which sort of separates the valence region from the core region. The region beyond r_c is treated as a valence region and within the r_c is core region. The value of r_c is chosen in such a way that the last node of the all electron wavefunction fall inside it. Pseudopotential and all electron wavefunction are identical outside the cutoff radius.

In the norm conserving pseudopotentials, the norm of all electron wavefunction in the core region (0 to r_c) remains conserved. Atoms like 2p, 3d and 4f have highly localized charge densities in the valence shell as well as in the core. The norm conserving pseudopotential is not much effective in reducing the number of plane waves required for representation. Another alternative to this is the ultrasoft pseudopotential. The ultrasoft pseudopotential generates the smoother wavefunction and reduces the size of required plane wave basis set, by increasing the value of r_c without sacrificing tranferability.

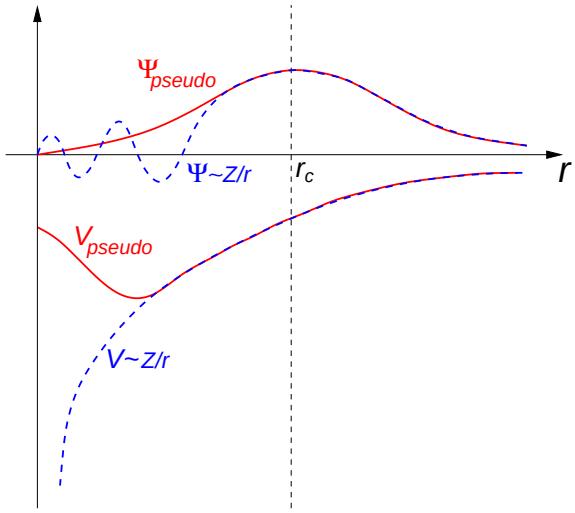

Figure 2.2: Schematic representation of all-electron (dashed lines) and pseudoelectron (solid lines) potentials and their corresponding wavefunctions. The radius at which all-electron and pseudoelectron value matches is designated r_c.

2.1.8 k-point sampling

Many calculations of crystals involve integrating periodic functions of a Bloch wave vector over the first Brillouin zone (BZ). There are infinite number of k-points in the first BZ. But since nearby k points contain similar information, the required physical properties of the system can be reproduced to desired accuracy by using the wavefunctions at a finite number of k-points usually generated by the Monkhorst-Pack in the first BZ. In other words, full BZ integral is approximated with a summation over a finite set of k-points. This approach is termed as a k-point sampling or BZ sampling.

The number of points required depends on the size and the features of the system. Insulators have filled bands that can be integrated using only a few special points. Symmetry can be used to further reduce the calculations since all independent information can be found from states with k in the irreducible BZ.

On the other hand, metals have bands that cross the Fermi energy where the Fermi-Dirac occupation varies rapidly. So, a metal requires careful integration for

those bands and requires much more k points for sampling than insulators or semiconductors. The number of k points can be reduced by smearing the Fermi surface discussed in next section.

2.1.9 Smearing

Smearing is needed for metals generally as the bands which crosses the Fermi level varies rapidly. There are various technique available for this purpose: Gaussian smearing, Fermi-dirac smearing, Methefessel-Paxton smearing and Marzari-vanderbilt cold smearing. In my thesis i have used Fermi-Dirac smearing function for calculations. The distribution for Fermi-Dirac function is given as:

$$f_i^{(k)} = \frac{1}{e^{(\varepsilon_i - \varepsilon_f)/K_B T_e} + 1}. \tag{2.19}$$

where $K_B T_e$ is a broadening parameter that is adjusted to avoid instabilities in the convergence of the self-consistent procedure.

2.1.10 Calculation of Stresses and Forces

The forces acting on the system greatly affects the molecular properties like stiffness of valence bonds, distortion in geometry ocurring due to the attraction and repulsion between the atoms etc. In order to get a correct information it is necessary to obtain the equlibirium structure of system. Force can be calculated from the first order derivative of energy with respect to displacement. This is quite a difficult task as it allows to calculate the forces at many different configurations and thus, it become difficult to calculate force constant for different bond in the system. The remedy to this problem is provided by Hellmann-Feynman forces theorem which states that the force on ion is minus the derivative of total energy of the system with respect

to the position of ion,

$$F_I = -\frac{dE}{dR_I} \tag{2.20}$$

where F_I is the force acting on Ith ion and E is the Born-Oppenheimer energy surface. It is designed to calculate the forces at a given configuration without the need for calculations at neighboring configurations.

For a system to be in equilibrium forces and stresses acting on the system should be zero. The stress acting on the system is obtained using the scheme of Nielsen and Martin. Stress ($\sigma_{\alpha\beta}$) is the derivative of energy with respect to strain tensor ($\epsilon_{\alpha\beta}$) per unit volume and is given by:

$$\sigma_{\alpha\beta} = -\frac{1}{\Omega}\frac{\delta E_{tot}}{\delta \epsilon_{\alpha\beta}}. \tag{2.21}$$

where α and β are cartesian coordinates.

2.2 Phonons

Crystal lattice possese long range translational order and all motions are ceased at absolute zero temperature. At T>0 K the ions vibrate with certain amplitude that depends on temperature. These thermal lattice vibrations can be considered as a collective motion of ions which can be populated and excited just like electrons. These excitations are phonons. Phonons greatly influence a wide variety of physical properties of materials: specific heats, thermal expansion, heat conduction, resistivity of metals, superconductivity etc. There are mainly two ways of calculating phonon modes: by displacing the particles according to desired pattern in a supercell of the required size (*frozen phonons*), and by perturbatively considering the displacements of the atoms in the unit cell and the appropriate vector in the phonon BZ (*linear response*). The linear response makes use of density functional

perturbation theory discussed below.

Density Functional Perturbation Theory

In this method, it is essential to calculate the second-order change in the DFT total energy (δ^2E) within the framework of density functional theory. The perturbation is induced by small displacement δR of ion from its equilibrium positions. This results in change in the external potential V_{ext}, which changes Ψ in the KS equation, and hence the charge density. The interatomic force constants (IFCs) are obtained using second order derivatives of ground state energy with respect to perturbation, i.e. ionic displacement,

$$K_{IJ} = \frac{\partial^2 E(\{\mathbf{R}\})}{\partial \mathbf{R}_I \partial \mathbf{R}_J} = \int \frac{\partial n(\mathbf{r})}{\partial \mathbf{R}_J} \frac{\partial V_{[R]}(\mathbf{r})}{\partial \mathbf{R}_I} d\mathbf{r} + \delta_{IJ} \int n(\mathbf{r}) \frac{\partial^2 V_{[\mathbf{R}]}(\mathbf{r})}{\partial \mathbf{R}_I \partial \mathbf{R}_J} d\mathbf{r} + \frac{\partial^2 E_N(\{\mathbf{R}\})}{\partial \mathbf{R}_I \partial \mathbf{R}_J} \tag{2.22}$$

The IFC depends on ground state charge density and its linear response to displacement of ion ($\frac{\partial n(r)}{\partial R_I}$). In the perturbation theory, Kohn-Sham equation is given as:

$$(H^{(0)}_{SCF} - \epsilon^{(0)}_i)|\phi^{(1)}_i\rangle + (V^{(1)}_{SCF} - \epsilon^{(1)}_i)|\phi^{(0)}_i\rangle = 0 \tag{2.23}$$

Here, $H^{(0)}_{SCF}$ is unperturbed Kohn-Sham Hamiltonian. $\epsilon^{(0)}_i$ and $\phi^{(0)}_i$ are the eigenvalues and eigenvectors of this Hamiltonian. The self-consistent Kohn-Sham effective potential is given at first order by:

$$V^{(1)}_{SCF}(\mathbf{r}) = V^{(1)}_{ext}(\mathbf{r}) + e^2 \int \frac{n^{(1)}(\mathbf{r}')dr'}{|\mathbf{r} - \mathbf{r}'|} + \int d\mathbf{r}' \frac{dV_{XC}(\mathbf{r})}{dn(\mathbf{r}')} n(\mathbf{r}') \tag{2.24}$$

Equation 2.28 and Equation 2.29 gives the change in the charge density given by:

$$\frac{\partial n(\mathbf{r})}{\partial \mathbf{R}_I} = 4Re \sum_{n=1}^{N/2} \psi_n^*(\mathbf{r}) \frac{\partial \psi_n(\mathbf{r})}{\partial \mathbf{R}_I} \tag{2.25}$$

Using Equation 2.24 and Equation 2.25 in Equation 2.22 we get force constant matrix and hence the phonon frequencies as eigenvalues of the dynamical matrix: $\frac{K_{IJ}}{\sqrt{M_I M_J}}$.

References

1. M. C. Payne, M. P. Teter, D. C. Allan, T. A. Arias and J. D. Joannopoulos, Iterative minimization technique for *ab initio* total-energy calculations: molecular dynamics and conjugate gradients, *Rev. Mod. Phys. 64, 1045-1097*

2. Richard M. Martin, *Electronic Structure: Basic Theory and Practical Methods*, Cambridge University Press, 2004

3. Jorge Kohanoff, *Electronic Structure Calculations For Solids and Molecues*, Cambridge University Press, 2006

Chapter 3

High Tunability of Work Function of (001) Surface of ReO_3 with O-vacancies

3.1 Introduction

Transition metal oxides exhibit a rich variety of properties such as ferroelectricity, magnetism, superconductivity, and have applications ranging from a catalyst, solar cells to electronic devices. Growth of their films can be controlled well [9], and they are considered as the materials for future electronic devices that can withstand high electric fields and power. Interfaces between two oxides are important not only in controlling the flow of charge, but can also open up many exotic phenomena. For example, a two dimensional electron gas is observed at the interface between two insulating oxides [2] with different polar structure, such as $LaAlO_3$ (LAO, polar) and $SrTiO_3$ (STO, non-polar), which essentially originates from the polar discontinuity at the interface [16]. The coexistence of superconductivity and magnetism, which are known to be mutually exclusive, is reported to exist at such an interface [3].

Oxygen vacancies are quite common in transition metal oxides, which also have remarkable influence on their properties. For example, oxygen vacancies occuring preferentially at the surface render magnetoelectric properties to nanocrystals of $BaTiO_3$ [10]. Experimental and theoretical studies have shown that oxygen vacancies in the (001) STO substrate, trapped during the growth of LAO layers on top, are responsible for the high mobility of carriers in the 2-D electron gas at the interface. This can not be explained based on the polar catastrophe mechanism alone [17, 18, 19]. Oxygen vacancies tune the work function of surfaces of transition metal oxides [13], can also lead to changes in the band offsets [20] relevant to charge transfer between electrode and oxygen vacancies. Resistive switching is another important area in which transition metal oxides can be used effectively in place of semiconductors [21, 22, 23].

Rhenium trioxide (ReO_3) is an unusual transition metal oxide, which exhibits excellent electrical conductivity that is comparable to a good metal like Cu. It occurs in the cubic perovskite ABO_3-type structure with a missing A site cation, and rhenium (Re) atom at the B site coordinated octahedrally by oxygen (O) atoms. It is an excellent candidate as a metallic oxide to be used as an electrode in oxide electronics. ReO_3 single crystal also acts as a catalyst for the metathesis reaction of olefins [24] and supported rhenium oxide acts as a catalyst for the selective oxidation of methanol [25]. Sanliang et al., [26] have theoretically shown that the molecular methanol adsorbed on ReO_3 surface can be easily dissociated, in agreement with experiments [25]. Work function of ReO_3 surface is important to both classes of its applications: electronics and catalysis.

ReO_3 nanocrystal has been effectively used in the surface enhanced Raman scattering (SERS) of adsorption of pyridine, pyrimidine and pyrazine [27]. ReO_3 is stable at fairly high temperatures at atmospheric presssure, but shows pressure induced structural phase transitions (at 3 GPa in the bulk form, and at 0.3 GPa in

its nanocrystalline form) [28, 29, 30, 31, 32, 33]. Such reduction in the transition pressure in nanocrystals can arise from the surface stresses, and it is important to understand the structure and electronic properties of ReO_3 surfaces. Tsukada et al., [34] used discrete-variational X_α methods to study various clusters of ReO_3 as models of the ReO_3 (001) surface, but a detailed study of vibrational spectra, electronic and structural properties of an extended surface has not been carried out yet.

Here, we present a detailed analysis of the structure and electronic properties of ReO_3 (001) surface with atomically different terminations (O-terminated and ReO_2-terminated), and discuss their stability. In the nominal ionic state of Re^{6+} in ReO_3 has one electron in the d-orbital, hence we explore the possibility of magnetism at its surface. We obtain insight into mechanism of pressure induced structural phase transitions of bulk and nanocrystals of ReO_3 through determination of phonon dispersion. We show that the work function of (001) surface of ReO_3 correlates inversely with its surface energy, and can be tuned remarkably through introduction of oxygen vacancies at the surface.

We first describe computational details in Section 3.2, and structural aspects of (001) surfaces in Section 3.3. Surface energies, work functions and tunability of work function with oxygen vacancies are discussed in section 3.4. We present electronic structure and its dependence on surface type in Section 3.5, and phonon dispersion in section 3.6. Finally we summarize and conclude in Section 3.7.

3.2 Computational details

Our calculations are based on density functional theory with ultrasoft pseudopotential [35] for oxygen core and a norm conserving pseudopotential [36] for rhenium

core as implemented in Quantum Espresso package [37]. We study (001) surfaces of ReO_3 with slabs of three different possible terminations: (a) type-A (ReO_2-terminated on both sides), (b) type-B (O- termintated on both sides) and (c) type-C (with O and ReO_2 termination on the two sides) as shown in Fig. 3.1 (Atomic planes are labelled using Roman numerals). Type A and B slabs are symmetric with identical surface termination while type-C is asymmetric. Slabs of type-A, type-B and type-C consist of 6.5, 4.5 and 4 unit layers respectively. The exchange-correlation energy of electrons is approximated with a local-density approximation (LDA) as parametrized by Perdew-Zunger [38]. Kohn-Sham wave functions are expanded in plane wave basis truncated with a kinetic energy cutoff of 30 Ry, and charge density with a cutoff of 200 Ry. We used $12 \times 12 \times 1$ Monkhorst-Pack k-point mesh for sampling integration of Brillouin zone (of surfaces supercells). Iterations for self-consistency in calculations are done till the total energies are converged within 10^{-6} eV/cell. The atomic positions are optimized until the Hellmann-Feynman forces on atoms become less than 0.03 eV/Å. The optimized lattice parameter of bulk ReO_3 is 3.77 Å, in reasonable agreement with its experimental value (3.75 Å) [39]. To avoid interaction between the periodic images of surfaces, we include a vacuum of 10 Å in the supercell. We have computed dynamical matrices corresponding to high symmetry points (Γ, X, M) in the Brillouin zone (BZ).

3.3 Structure of (001) surfaces

Examining geometry of relaxed structures of three models of slabs, we find that the structural relaxation is more pronounced at the surfaces, as expected. Relaxation (seen as changes in the Re-O bond lengths w.r.t. the bulk bond length) is more pronounced for the O-terminated surface in comparison with the ReO_2-terminated surface. The Re-O bond length decreases by 7.5% for the type-B surface while only

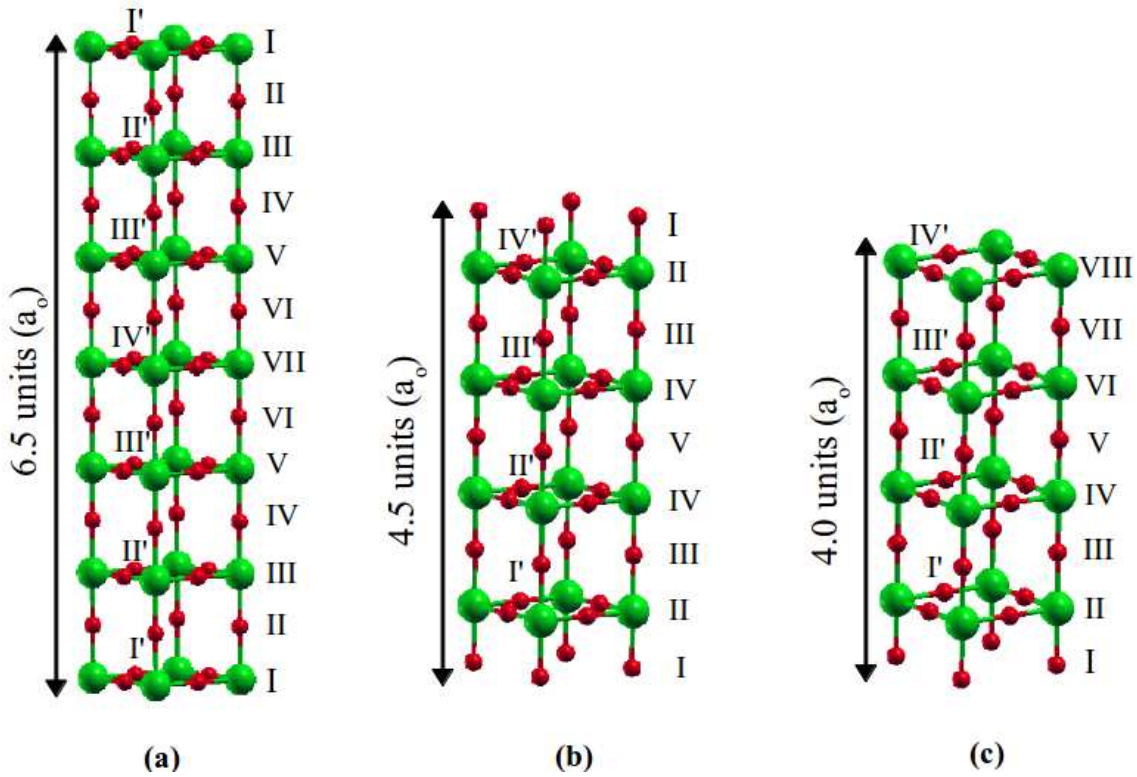

Figure 3.1: Configurations of slabs of ReO_3 with (a) ReO_2-termination (type-A), (b) O-termination (type-B), (c) Mixed O and ReO_2-termination (type-C). Red and green balls are oxygen and rhenium atoms respectively.

by 2.64% for type-A surface. Reduction in the Re-O bond length at the surface for type-A and type-B surface is a result of movement of atoms present at surface and in sub-surface plane in opposite directions. The type-C configuration shows a mixed effect i.e, for ReO_2-terminated surface Re-O bond length contracts by 3.1% while it is 7.45% for O-terminated surface. Being asymmetric one, it undergoes different changes at the two sides: both surface and sub-surface atoms move in the same direction (towards the bulk or away from the vacuum) at ReO_2-terminated plane, and the movement of atoms (at the surface and sub-surface) are opposite in direction at O-terminated plane. The trend in changes in bond length is shown in Table 3.1.

Reduction in the Re-O bond length at the surface causes elongation of the bond

Table 3.1: The percentage change in Re-O bond length (along z-direction) of slabs of ReO_3(w.r.t. equilibrium bond length of 1.884 Å). Layers are labelled with roman numbers starting from the surface (see Fig. 3.1).

Planes	Type-A	Type-B	Type-C
I-II	-2.64	-7.50	-7.45
II-III	1.07	6.56	6.98
III-IV	0.07	-1.98	-2.49
IV-V	0.07	0.61	-0.04
V-VI	-0.65		-0.16
VI-VII	0.54		1.56
VII-VIII			-3.13

length at the next atomic plane away from the surface. Similar behavior was reported for the surfaces of $CaTiO_3$, $SrTiO_3$ and $BaTiO_3$ [40, 41, 42]. For the type-A and type-C (ReO_2-plane in particular) surfaces, Re atoms move towards the bulk (into the slab) and O atoms move outwards (towards the vacuum). O atom at the type-B surface moves towards the bulk. Re-O bonds parallel to the surface undergo elongation by 0.75% and 0.89% at the type-A and type-C surfaces respectively and the changes are not significant in the inner atomic planes. We do not see contraction for the Re-O bonds parallel to the surface. For completeness, we have also shown changes in interlayer spacing (distance between two oxygen atoms present at the centre of axis) w.r.t. optimized bulk lattice constant in Table 3.2.

Table 3.2: Change in the inter layer spacing in percentage with respect to optimized lattice constant 3.77 Å. Note: Distance is between oxygen atoms present along the central axis and measured along z-direction.

$\Delta d_{i,j}$	Type-A	Type-B	Type-C
$O_{I'-II'}$	4.84	-1.45	-1.71
$O_{II'-III'}$	0.40	-0.78	-0.07
$O_{III'-IV'}$	0.14		5.31

3.4 Surface energy (γ_s) and work function (ϕ)

The surface energy is defined as the energy required to create a new surface, by cleaving a bulk crystal or as the excess energy due to fewer bonds at the surface in comparison with the bulk. We determine the surface energies of the three configurations of slabs using equations (1), (2), and (3) for type-A, type-B and type-C slabs respectively.

$$\gamma_s = \frac{1}{2a^2}(E_{slab} - 7E_{bulk} + 0.5E_{O_2}) \tag{3.1}$$

$$\gamma_s = \frac{1}{2a^2}(E_{slab} - 4E_{bulk} - 0.5E_{O_2}) \tag{3.2}$$

$$\gamma_s = \frac{1}{2a^2}(E_{slab} - E_{bulk}) \tag{3.3}$$

where, E_{slab}, E_{bulk}, and E_{O_2} are the total energies of the slab, bulk ReO_3 and an oxygen molecule, a is the lattice constant and $\frac{1}{2}$ accounts for the two surfaces created in the slab configuration. The type-B has the lowest surface energy of 0.86 J/m^2, indicating its high stability. In contrast, the type-A has the highest surface energy of 4.77 J/m^2, and hence is the least stable. γ_s of the type-C configuration is energetically close to average of those in type-A and type-B slabs, with an average surface energy of 2.50 J/m^2.

The work function is the minimum energy required to remove an electron from the Fermi level of a metal to a point in vacuum at infinity and has been obtained

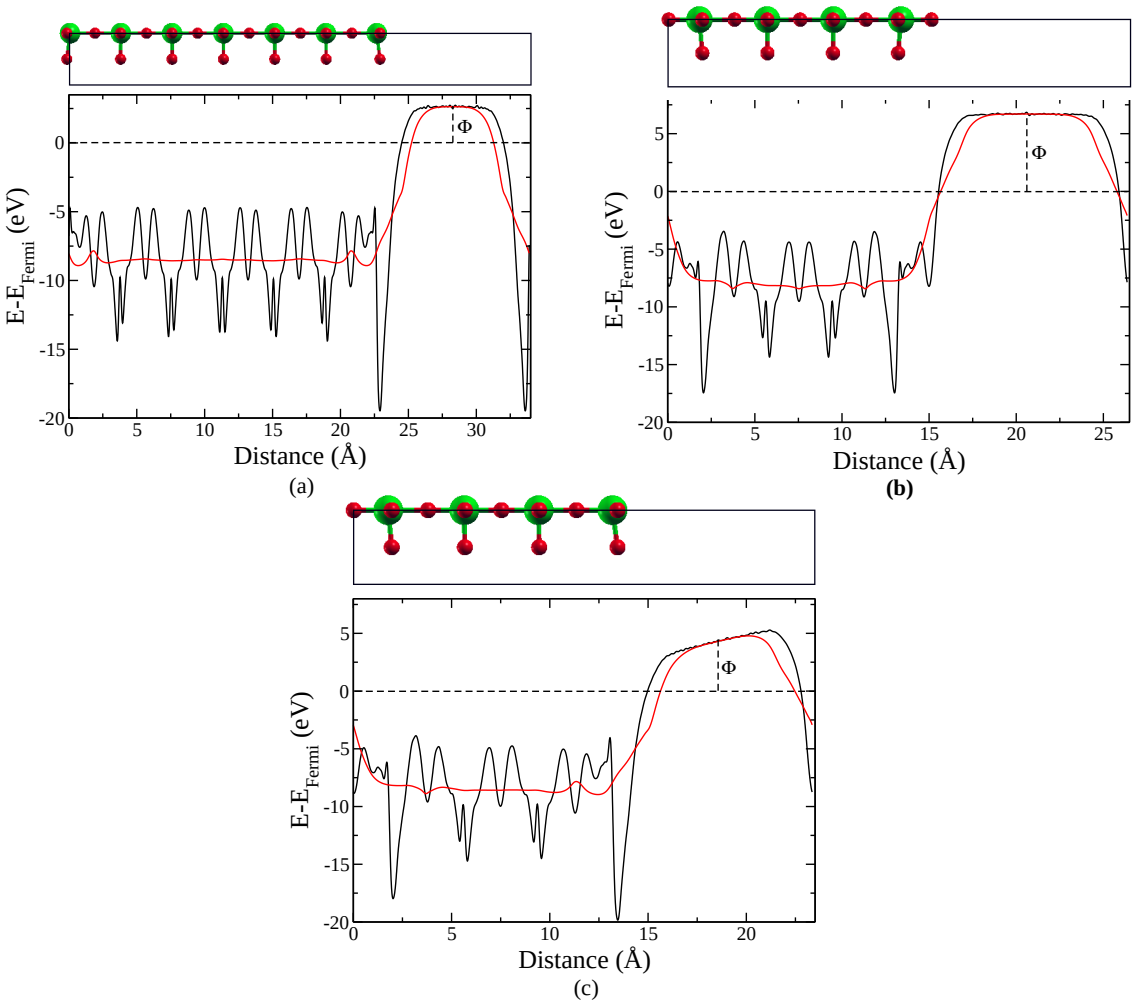

Figure 3.2: Variation in potential energy along the direction perpendicular to (a) ReO_2-terminated, (b) O-terminated, and (c) mixed O and ReO_2-terminated slabs of ReO_3. Red and green circles are oxygen and rhenium atoms respectively.

using the following expression:

$$\phi = V_{vacuum} - E_{Fermi} \tag{3.4}$$

where, V_{vacuum} is the average potential in the vacuum region, and E_{Fermi} is the Fermi level. Here, the potential includes bare nuclear, Hartree and exchange-correlations potentials. From the variation in potential along the direction perpendicular to surfaces of ReO_3 (shown in Fig. 3.2.), estimates of the work function of type-A,

type-B and type-C slabs are 2.6 eV, 6.8 eV and 4.4 eV respectively. The work functions follow a reverse trend as of the surface energy i.e, the slab with lowest surface energy has the highest work function; the work function correlates with the stability of the surface. For a ready comparison, we have tabulated γ_s and ϕ in Table 3.3.

Table 3.3: Surface energies and work functions of ReO_3

Slabs	Surface energy (J/m^2)	Work Function (eV)
Type-A	4.77	2.6
Type-B	0.86	6.8
Type-C	2.50	4.4

There is a non-zero slope in the electrostatic potential in vacuum for the type-C configuration [Fig. 3.2(c)], indicating that the type-C is polar in nature and there is an electric field of -4.52×10^9 V/m. A linear fit of the dependence of this electric field on vacuum thickness yields the following expression:

$$E_d(d_v) = \frac{1}{0.28d_v - 0.061} \tag{3.5}$$

Here, d_v is the vacuum thickness in nm and E is an electric field in V/nm. The equation shows that the electric field vanishes as the vacuum thickness becomes infinitely large. So, the slope in Fig. 3.2(c) will tend to zero as vacuum thickness approaches infinity.

As oxygen vacancies are commonly present in transition metal oxides, we have investigated the work function as a function of oxygen vacancies on the most stable (oxygen terminated) surface. We consider different surface concentration of oxygen vacancies by using supercell in the $ab-$plane (for example, $\sqrt{2} \times \sqrt{2}$, 2×2). We note that the ReO_2-terminated surface corresponds to 100 % oxygen vacancies in the O-terminated slab. We find a significant decrease in the work function with

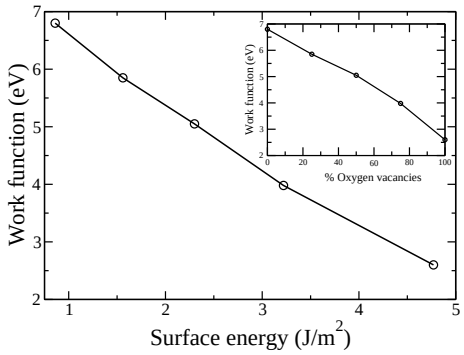

Figure 3.3: Variation of work function with surface energy at different concentration of oxygen vacancies. Inset shows the trend of change in work function as a function of oxygen vacancies concentration.

increase in concentration of oxygen vacancies at the surface (see Fig. 3.3). Such decrease in work function is due to (a) reduction in oxidation state of Re due to oxygen vacancies, and (b) formation of electric dipoles at the surface. Indeed, oxygen vacancies have an energy cost, and hence result in increase in the surface energy. The stability of (001) surface of ReO_3 thus reduces with oxygen vacancies, and the correlation of work function with stability is quite clear in our results (Fig. 3.3). The work function directly influences the energy barriers at interfaces, and in the case of ReO_3, Schottky barrier at a metal-semiconductor interface can thus be tuned with oxygen vacancies. These results also have remarkable consequences to electronics based on the 2-D electron gas forming at the interface of two insulating oxides. In particular, our work highlights drastic changes that can occur in the work function of an oxide due to oxygen vacancies, and provides a mechanism to understand sensitivity of the 2-D electron gas to growth conditions.

3.5 Electronic structure and Density of States

The electronic structure calculated along the high symmetry lines in the BZ is shown in Fig. 3.4. Electronic structure of bulk ReO_3 [Fig. 3.4(a)] exhibits flat bands in the

lower part of conduction band in the Γ-X region and in the valence band minima ranging along X-M segment. The most striking feature in the electronic structure of surfaces shown in Fig. 3.4(b)-3.4(d) is the presence of many flat bands; and so the wavefunctions are expected to be localized at the surface. Previous studies on the electronic structure of surfaces have reported the presence of flat bands. For eg; the lowest conduction band of $SrTiO_3$ (100) surface is flat betweem Γ and X points [43]. In case of (001) surface of cubic $BaMnO_3$, the top valence band is flat between Γ and X points [44].

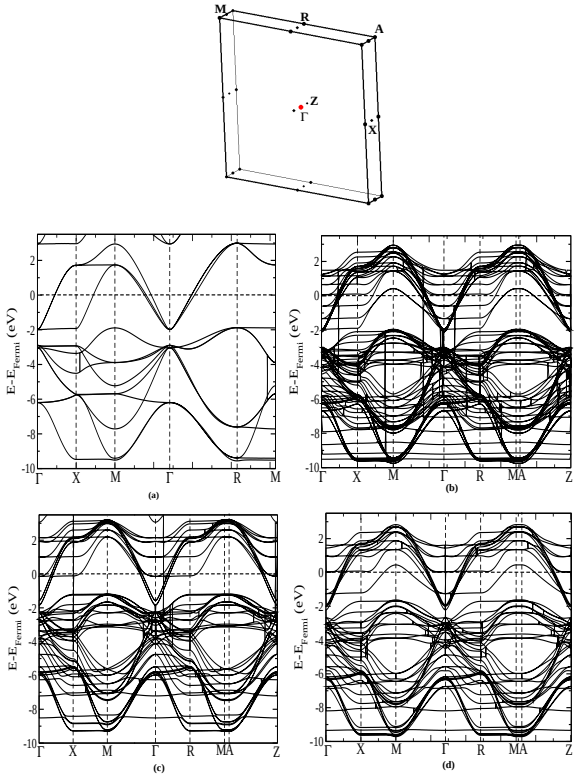

Figure 3.4: Electronic structure of (a) bulk, (b) ReO_2-terminated, (c) O-terminated, (d) mixed O and ReO_2-terminated surfaces. Brillouin zone of slab is given at the top.

The partial density of states (PDOS) of bulk ReO_3 (Fig. 3.5) and the layerwise PDOS of three slabs (Fig. 3.6) show that their valence band mainly constitutes O-2p orbitals and the conduction band has Re-5d states. PDOS of bulk ReO_3 (Fig.

3.5) shows that the O-2p orbital (p_z) pointing towards the metal form σ-bond while those perpendicular to M-O-M forms π-bond. The hybridization between metal and oxygen is bonding in valence band whereas, it is non-bonding in the conduction band. The same prediction for bulk ReO_3 was given by Cora [45] and Stachiotti [46]. The widths of conduction and valence bands of bulk ReO_3 are about 4.7 eV and 8.3 eV respectively. Previous reported values for width of conduction and valence bands are 5.0 eV and 8.4 eV respectively [45, 46], so our results are in close agreement with their result. Due to lowering of symmetry O-2p and Re-5d orbitals are no longer degenerate in surfaces. It is evident from Fig. 3.6(a)-3.6(c) that the PDOS peaks of p_x, p_y and p_z orbitals of the oxygen atoms coincide with those of the PDOS peaks of Re-5d orbitals indicating a strong hybridization between these orbitals. This leads to the lowering of energy of e_g orbitals relative to t_{2g}, opposite to that expected in octahedral crystal field splitting. The same is seen for bulk ReO_3 (Fig. 3.5) and has been discussed by Stachiotti *et al* [46]. The PDOS of bulk ReO_3 shows the

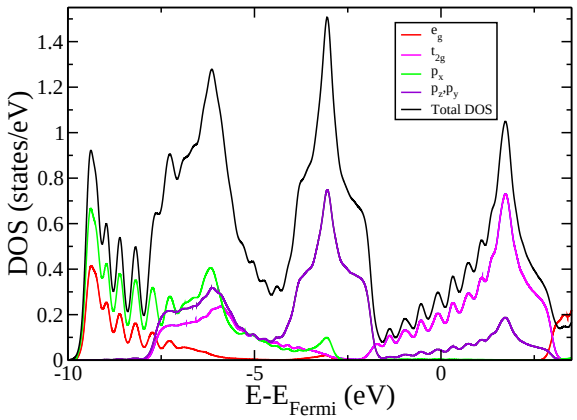

Figure 3.5: Total and projected density of states of bulk ReO_3.

contribution of t_{2g} orbitals at the Fermi level (Fig. 3.5). The PDOS of slabs shows that t_{2g} and d_z^2 orbitals of Re are dominant at the Fermi level at the surface layer of type-A, while d_{xy} orbitals of Re dominates the Fermi level at the sub-surface

plane in type-B. The type-C shows mixed properties of type-B and type-A, so the layers close to ReO_2-plane at the surface show the behavior of type-A, while those near to O-plane at surface shows the behavior of type-B surface. Unoccupied states comprising of e_g orbitals are found in bulk ReO_3 at higher energy, but it is found in surface layers at energies lower than that in bulk. The removal of oxygen at the surface causes an increase in the nucleus field which leads to the lowering of energy of Re-6s states above Fermi level as compared to those in bulk ReO_3 and in sub-surface planes.

Contribution of Re-5d states to bands at the Fermi level is dominant [Fig. 3.6(a)-3.6(c)] and so work function of ReO_2-terminated surface is low as compared to the O-terminated surface as O-2p states are deep below the Fermi level. Kanishka *et al,* [47] reported that the ReO_3 nanocrystal shows weakly paramagnetic behavior at ordinary temperatures and magnetic hysterisis at low temperatures when the size of particle is small, noting that Re in ReO_3 has one electron in d-orbital and may show some magnetization. We explored a possible magnetization, and find that the type-A surface exhibits weak magnetization whereas, there was no magnetization in type-B surface as it lacks any Re at the surface. The difference in the occupancy of up-spin and down-spin in Re atoms at surface leads to weak magnetization at the surface. The same is evident in spin density distribution, where spins are mainly localized around the Re atoms at the surface (Fig. 3.7). The type-C slab don't exhibit any magnetization, which is probably due to its polarity and the presence of O-terminated surface at one of its ends.

3.6 Phonons

To determine vibrational signatures and assess the structural stability of ReO_3 surface, we obtain phonon dispersion along the high symmetry lines of the Brillouin

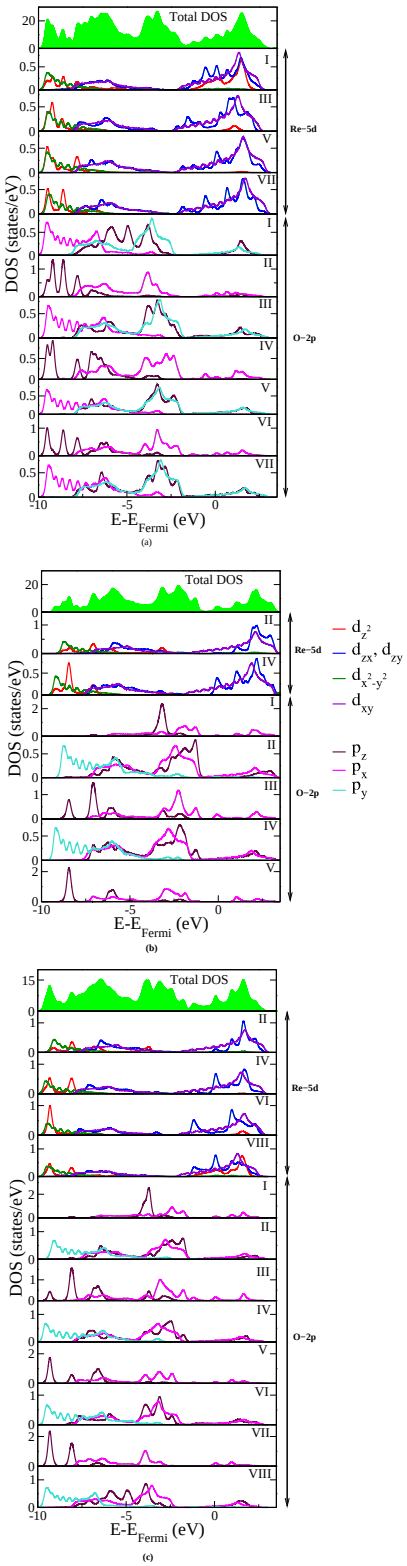

Figure 3.6: Total and projected density of states of (a) ReO_2-terminated, (b) O-terminated, and (c) mixed O and ReO_2-terminated slabs of ReO_3. Note: O-2p orbitals in II,IV,VI for Fig (a), I, III, V for Fig. (b) and I, III, V and VII for Fig. (c) have degenrate p_x and p_y states.

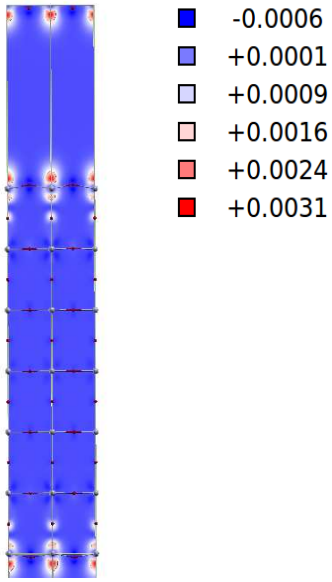

Figure 3.7: Spin density distribution of ReO_3 slab with ReO_2-termination.

zone for the most stable surface (type-B) [Fig. 3.8(a)]. It shows imaginary modes of 36.71i cm^{-1} at (100) $\frac{\pi}{a}$ (X-point), suggesting that the structure is weakly unstable at nano-scale. The bulk ReO_3 undergoes pressure induced phase transitions through cubic (0-3 GPa), monoclinic (3-12 GPa), VF_3-type structure (above 12 GPa) and extremely hard rhombohedral phase (above 38 GPa) [29]. Experimentally ReO_3 nanocrystal exhibits pressure induced phase transition from cubic I structure (pm3m) at the ambient pressure which changes to a monoclinic structure (C2/c) around 0.3 GPa, and it transforms to rhombohedral I structure (R3c) around 6.7 GPa and to rhombohedral II structure around 20.3 GPa [28]. Thus, transition pressures are lower in nanocrystals than in the bulk. The phonon dispersion [Fig. 3.8(a)] shows soft unstable mode around X-point of the slab which is relevant to pressure induced phase transition in nanocrystals of ReO_3. The unstable mode involves the in-plane and out-of plane displacement of oxygen atoms present in both ReO_2 and O-planes [Fig. 3.8(b)] amounting to ReO_6 rotation; such ReO_6 octahedral rotations are also known to be relevant to the phase transition of the bulk ReO_3, where they correspond to M_3 phonons (at wave vector (110)$\frac{\pi}{a}$). Here, these instabilities are

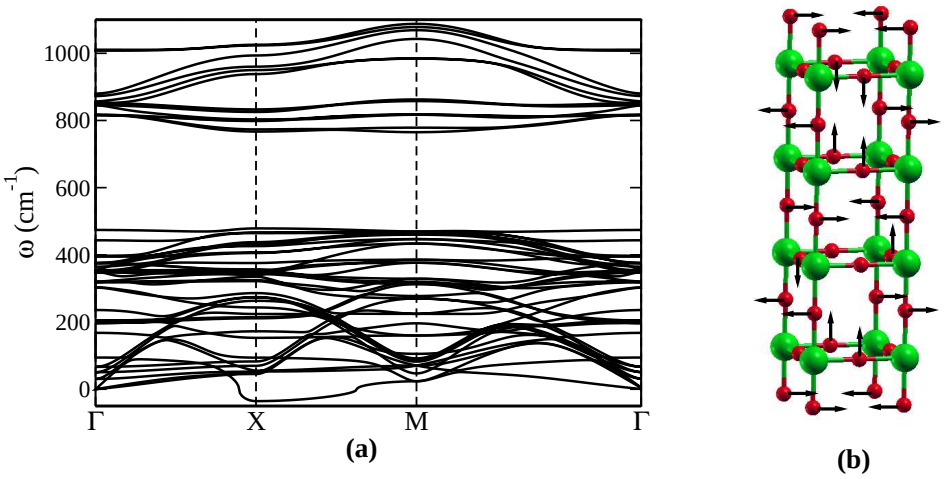

Figure 3.8: (a) Phonon dispersion along high symmetry lines of the Brillouin zone, and (b) atomic displacements associated with unstable mode at X-point of O-terminated slab.

strengthened by the surface and should manifest in transitions at lower pressure in nanocrystals of ReO_3 [28]. Such size dependence of pressure-induced phase transitions can be understood in terms of the stress created by the surface as a result of lower coordination of O and shorter Re-O bond lengths. This mimic compressive normal stress, which offsets (lower) the transition pressures as seen in experiment [28].

3.7 Summary

We have investigated three different configurations (type-A, type-B and type-C) of (001) surfaces of ReO_3. Contraction of about 7.50% and 2.64% in Re-O bond length results at the O-terminated surface and ReO_2-terminated surface respectively. The type-C configuration is asymmetric, polar in nature, and the electric field associated with it goes to zero as the vacuum thickness tends to infinity. Electronic structure of ReO_3 surfaces contains many flat bands associated with electronic states localized at the surface, and Re-5d orbitals dominate the states at the Fermi level and result

in a weak magnetization found at the ReO_2-terminated (001) surface. Structural instabilities involving ReO_6 rotations are further strengthened by the stresses created at the surface, and provide a possible explanation for the observed reduction in transition pressure in nanocrystals relative to bulk.

Based on the surface energies, O-terminated surface is the most stable (001) surface of ReO_3. The surface with the lowest surface energy (greatest stability) has the highest work function. We have demonstrated that the work function of ReO_3 (001) surface can be tuned by controlling the concentration of oxygen vacancies at its surface. Our work highlights the remarkable consequences oxygen vacancies can have to oxide heterostructures based electronics, and provide a mechanism of their effect on the work function to understand sensitivity of their interfacial properties to oxygen vacancies, and hence the growth conditions such as oxygen pressure. Thus, it should be possible to engineer the work function of an oxide through control on oxygen vacancies.

Chapter 4

Adsorption of pyridine on ReO_3 and SERS

4.1 Introduction

Surface Enhanced Raman Spectra (SERS) is a technique which is based on significant advancement in Raman signal when a molecule is in vicinity of a metal surface. The typical enhancement factor observed in SERS ranges from 10^4 to 10^8. There are mainly two mechanisms responsible for SERS one involves enhancement in electric field at molecular position due to excitation of a plasmon at the surface (electromagnetic enhancement) [48, 49, 50]. The second involves chemical enhancement which arises because of chemical interaction such as charge transfer between molecule and substrate [51, 52]. The combination of electromagnetic and chemical enhancements is typically responsible for SERS.

While electromagnetic enhancement plays a dominant role, chemical enhancement is of the order of 10-10^2 [53]. There are other factors like surface roughness, size and shape of the particle, the nature of adsorbate and wavelength which affect the surface enhancement to some extent. Metals like Ag, Au, and Cu are primarily

used as a substrate but Tian *et. al.*, reported that the transition metals like Pt, Ru, Rh, Pd, Fe, Co, Ni, and their alloys can be also used as a substrate [54]. At the junction of nanoparticles, molecule shows a large enhancement of order 10^{14}-10^{15} [55, 56].

ReO_3 is a metallic oxide with its conductivity comparable to that of copper. Kanishka *et. al.* [27], have shown SERS for adsorption of pyridine (Py) on ReO_3 nanocrystal with enhancement factor of order 10^5-10^6, which is quite large. According to them, Raman signals enhancement is due to the bonding interaction between Py and metallic ReO_3. On the basis of Raman spectra they predict that molecule adsorbed in a flat-on configuration. Theoretically, we have shown that both chemical and electromagnetic enhancements are resposible for this behavior. Py adsorbs by forming bond with the oxygen atom at the surface. Subsequent elongation of C-N bond of Py results in softening of phonon modes, i.e. the red shifts observed in Raman spectra. Also, the interaction between Py and surface leads to blue shift in ring stretching mode.

We have organize this chapter as follows: Computational details are discussed in section 4.2, followed by results and dicussion in section 4.3. Finally we conclude in section 4.4.

4.2 Computational details

Our first-principles calculations are based on density functional theory (DFT) as implemented in Quantum Espresso package [37]. We have used a local density approximation (LDA) to exchange-correlation energy with Perdew-Zunger parameterized form [38]. We employ periodic boundary conditions with 3 x 3 x 4 supercell (155 atoms) of ReO_3 with a coverage of 9.38 mg of Py per g of ReO_3, and include a

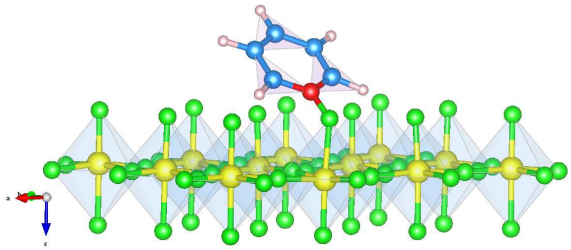

Figure 4.1: Stable configuration of pyridine on ReO_3 surface.

vaccum of 17 Å, in the direction perpendicular to ReO_3 slab to keep interactions between periodic images low. We use uniform mesh of 4 x 4 x 1 k-points in sampling integrations over Brilloiun zone, and smear the occupation numbers of electronic states with Fermi-Dirac distribution and smearing width (k_BT) of 0.014 eV. We relax the structure to minimize energy until the Hellmann-Feynman forces on each atom are less than 0.03 eV/Å in magnitude. We have used density functional perturbation theory to calculate zone center phonons for an isolated (free) Py molecule and Py of structure frozen from the adsorbed configuration to determine effects on its phonons arising from adsorptive interaction.

4.3 Results and Discussion

We use many initial configurations of Py on ReO_3 surface and find the lowest energy stable geometry for the adsorption of Py on ReO_3 surface (see Fig. 4.1). Py tilts a bit towards the surface and adsorbs by making bond with the oxygen atom, with N-O bond length of 1.35 Å clearly indicating chemisorption. The adsorption energy (E_A) is calculated using:

$$E_A = E_{Complex} - E_{ReO_3} - E_{Py}, \tag{4.1}$$

where, $E_{Complex}$, E_{ReO_3} and E_{Py} are the total energies of the complex, ReO_3 slab and isolated Py molecule respectively. Our results reveal that $E_A < 0$ (i.e, -170.80

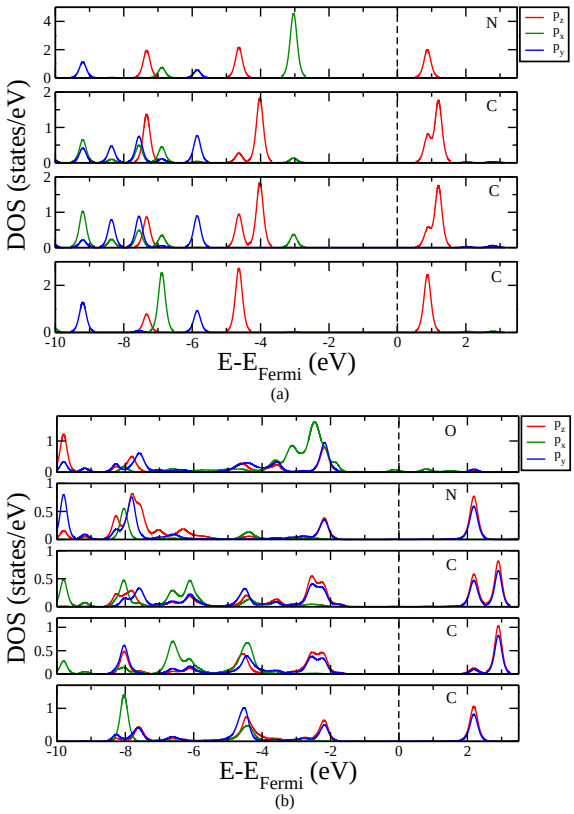

Figure 4.2: Projected density of states of (a) isolated pyridine, and (b) pyridine after adsorption. C atoms have been labelled in anticlockwise direction starting with N atom in Py.

kJ/mol or -1.77 eV). We have compared the adsorption energy of Py on Au and Cu substrates obtained using DFT calculation with our result in Table 4.1. It is clear that adsorption energy of Py on ReO_3 is quite large as compare to that on Au and Cu.

Table 4.1: Adsorption energies (in eV) of Py on Au (111), Cu(111) and ReO_3 (001) surface.

	E_{ad}	Ref.
Cu/Py	-0.06	[57]
Au/Py	-0.06	[57]
ReO_3/Py	-1.77	-

Upon adsorption, Re-O bond (O to which nitrogen is attached) got elongated by 6.77% while rest of the bonds at the surface contract by about 7%. There is also an

increase of about 1% in the C-N bond length of Py after adsorption. This is primarily due to the charge transfer between C and N atoms after adsorption. In order to check the charge transfer between adsorbate and substrate, we have estimated Lödwin charges as implemented in Quantum espresso using following relation:

$$\delta q = q^{Py}_{ReO_3-Py} q^{Py}_{frozen} \tag{4.2}$$

where, δq is the charge transfer, $q^{Py}_{ReO_3-Py}$ is the total charge on Py in ReO_3-Py system and q^{Py}_{frozen} is the total charge on frozen Py. δq comes out to be -0.8348 e, which implies that the charge is transferred from molecule to surface, maximum charge being transferred from N atom of Py. Projected density of states in [see Fig. 4.2(b)] shows the formation of a covalent bond between the p-orbitals of nitrogen and oxygen atoms at the surface. Same is also evident in the charge density plot in Fig.

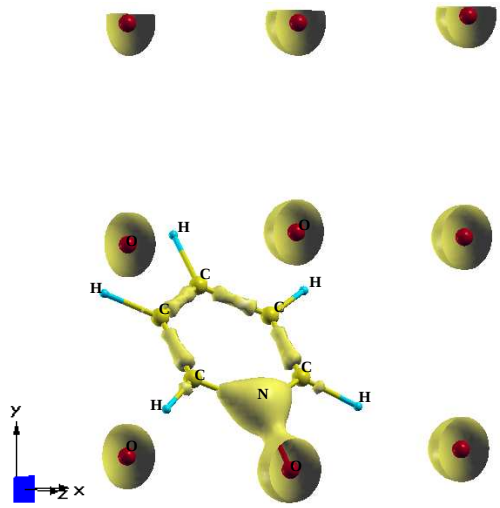

Figure 4.3: Charge density plot of adsorption of pyridine on surface.

4.3. It is clearly seen from Fig. 4.2 that the LUMO state of Py shift towards higher energy after adsorption. HOMO-LUMO gap obtained in isolated Py and of Py of structure frozen after adsorption (shown in Table-4.2) shows a large reduction in HOMO-LUMO gap upon adsorption confirming that chemical interaction is indeed

significant.

Table 4.2: HOMO-LUMO energies (in eV) and the gap Δ of pyridine before and after adsorption.

	Pyridine (isolated)	Pyridine (frozen)
HOMO	-5.5959	-5.3303
LUMO	-1.6844	-1.7994
Δ	3.9115	3.5309

From the electrostatic potentials shown in Fig. 4.4, electric field is estimated to be 2.52 V/Å which is quite large. Thus, we believe that both electromagnetic and chemical enhancements are responsible for the observed SERS signal in experiments [27].

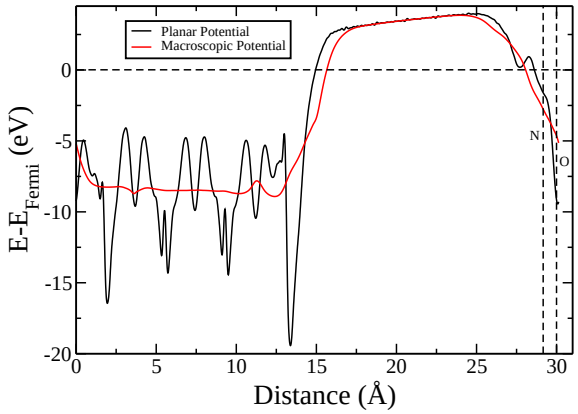

Figure 4.4: Potentials obtained after adsorption of pyridine on the surface in a direction perpendicular to the surface.

Raman spectra obtained experimentally [27] show that, ring stretching mode at 1582 cm^{-1} shifts to higher frequency after adsorption whereas greater red shift is observed for the modes at 1068 cm^{-1} (ν_{18a}) and 991 cm^{-1} involving symmetric ring breathing (ν_1, A_1). We obtain zone centre phonons of Py before and after adsorption and compare it with experimental results. Qualitatively, our estimates follow the trend seen in experiment (Table 4.2). From this, the observed softening of Raman modes after adsorption is basically due to the elongation of the C-N bond length.

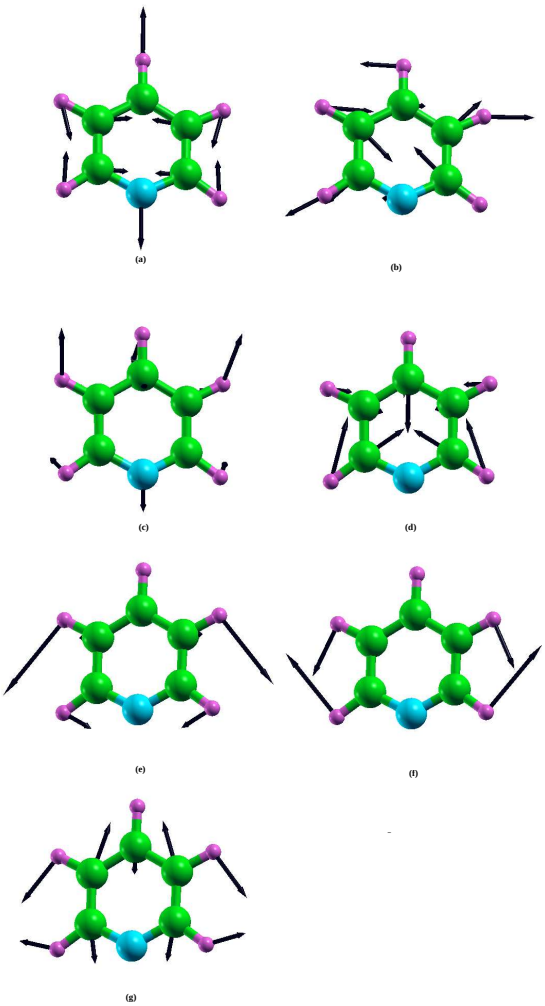

Figure 4.5: Phonon modes of pyridine adsorbed on surface (a) 590.51 cm^{-1} (asymmetric ring breathing mode) (b) 640.77 cm^{-1} (ring in plane deformation) (c) 974.81 cm^{-1} (symmetric ring breathing) (d) 1022.23 cm^{-1} (trigonal ring breathing) (e) 1034.60 cm^{-1} (ν_{18a}, A_1) (f) 1159.48 cm^{-1} (C-H in plane deformation) (g) 1593.46 cm^{-1} (ring stretching)

The interaction between Py and surface leads to blue shifting in asymmetric ring breathing [Fig. 4.5(a)] and ring stretching mode [Fig. 4.5(g)]. Large enhancement in the Raman signals of trigonal ring breathing mode and symmetric ring breathing mode is observed. Fig. 4.5(c) and Fig. 4.5(d) show that these modes involve displacements of atoms that are along z-direction, which couple with the large surface electric field generated along z-direction, leading to enhancement in the observed intensity. Also, N atom moves towards the surface in the symmetric mode, and this

Table 4.3: Frequencies of phonon modes (in cm^{-1}) obtained theoretically and Raman spectra positions (in cm^{-1}) obtained experimentally of pyridine before adsorption and after adsorption on the surface of ReO_3.

Before adsorption		After adsorption	
Theory	Experiment	Theory	Experiment
590.83	608	590.51	610
647.33	650	640.77	632
984.33	991	974.81	962
1029.18	1031	1022.23	1006
1042.33	1068	1034.60	1027
1182.95	1214	1159.48	1201
1588.52	1582	1593.46	1628

could be another reason for the enhancement observed in the intensity of this mode.

4.4 Summary

Our density functional theory calculations suggest that the enhancement in Raman signal observed in Py on ReO_3 nanocrystal is due to both (a) electromagnetic enhancement evident in the potential profile and (b) formation of strong covalent bond between N and O atom present at the surface (chemical enhancement) involving the charge transfer between N and O atom at surface. Py tilts a bit towards the surface during adsorption. Red shift observed in the frequency is due to the elongation of C-N bond length. Interaction between Py and surface also leads to blue shifting observed in ring stretching mode. Large reduction seen in the HOMO-LUMO gap of Py upon adsorption confirms that chemical enhancement is quite significant and may be relevant to SERS observed experimentally. The displacement of atoms along z-direction couples well with surface electric field, leading to a large enhancement in the intensity for trigonal and symmetric ring breathing modes.

Chapter 5

Conclusion

Using first-principles calculations based on the density functional theory, we have determined electronic, structural and vibrational properties of (001) surface of ReO_3, and its adsorptive interaction with pyridine.

In the **first part**, we have carried out a detailed study of various properties of ReO_2-terminated and O-terminated surface with symmetric terminations. As expected, structural relaxation is more pronounced at the surface particularly for the surface with O termination. Re-O bond length contracts by 7.5% at O-termination while it reduces by 2.45% at ReO_2-terminated surface. We also considered the surface with mixed O and ReO_2-termination, *i*.e. asymmetric surface. Asymmetric surface is polar in nature with weak electric field in the vacuum which tends to zero as the vacuum thickness tends to infinity. The flat bands in the electronic structure of ReO_3 surface may relate to delocalized electronic states. Weak magnetization is found at ReO_2-terminated surface due to dominance of Re-5d states at Fermi level. ReO_6 octahedral rotation leads to structural instability at the surface, and stresses created at surface enhance it further. So, phase transiton in nanocrystalline form of ReO_3 occurs at lower pressure as compared to that in its bulk form.

On the basis of surface energy, O-terminated surface is the most stable of all.

A linear correlation exists between surface energy and work function. We predict a drastic change in work function from 7 to 3 eV by controlling the concentration of oxygen vacancies at the surface (O-terminated). Thus, we have shown that the work function of oxides can be engineered by controlling the oxygen vacancies percentage through oxygen pressure during growth of a film.

ReO_3 nanocrystal causes surface enhanced Raman spectra on adsorption of molecule. In the **second part** of thesis, we study adsorption of pyridine on the O-terminated (001) surface. We find that pyridine binds strongly with the surface (N-O bond length 1.35 Å) through its nitrogen atom. The molecule tilts slightly towards the surface upon adsorption. The large surface electric field is present near the molecule. On the basis of these results we argue that both electromagnetic and chemical factors lead to enhancement in the Raman signal observed experimentally.

Bibliography

[1] P. Zubko *et al.*, Annual Review of Condensed Matter Physics **2**, 141 (2011).

[2] A. Ohtomo and H. Y. Hwang, Nature **427**, 423 (2004).

[3] J. A. Bert *et al.*, Nat. Phys. **7**, 767 (2011).

[4] E. Bousquet *et al.*, Nat. Letters **452**, 732 (2008).

[5] W. F. Maier, Angewandte Chemie International Edition in English **29**, 1074 (1990).

[6] R. Matzdorf *et al.*, Science **289**, 746 (2000).

[7] N. Bickel, G. Schmidt, K. Heinz, and K. Müller, Phys. Rev. Lett. **62**, 2009 (1989).

[8] A. Munkholm *et al.*, Phys. Rev. Lett. **88**, 016101 (2001).

[9] M.-G. Kim, M. G. Kanatzidis, A. Facchetti, and T. J. Marks, Nat. Mater. **10**, 382 (2011).

[10] R. V. K. Mangalam *et al.*, Solid State Commun. **149**, 1 (2009).

[11] Chen, Yu, and S. B. Adler, Chemistry of Materials **17**, 4537 (2005).

[12] Y.-M. Kim *et al.*, Nat. Mater. **11**, 888 (2012).

[13] M. T. Greiner *et al.*, Adv. Funct. Mater. **22**, 4557 (2012).

[14] F. Razavi, Z. Altounian, and W. Datars, Solid State Communications **28**, 217 (1978).

[15] U. K. Sur and J. Chowdhary, Current Science **105**, 923 (2013).

[16] N. Nakagawa, H. Y. Hwang, and D. A. Muller, Nat. Mater. **5**, 204 (2006).

[17] Z. Zhong, P. X. Xu, and P. J. Kelly, Phys. Rev. B **82**, 165127 (2010).

[18] G. Herranz *et al.*, Phys. Rev. Lett. **98**, 216803 (2007).

[19] Y. Li *et al.*, Phys. Rev. B **84**, 245307 (2011).

[20] E. Cho and S. Han, Microelectron. Eng. **88**, 3407 (2011).

[21] M. J. Rozenberg *et al.*, Phys. Rev. B **81**, 115101 (2010).

[22] J. Celinska, C. McWilliams, C. Paz de Araujo, and K.-H. Xue, J. Appl. Phys. **109**, (2011).

[23] J. H. Hur *et al.*, Phys. Rev. B **82**, 155321 (2010).

[24] N. Tsuda and A. Fujimori, J. Catal. **69**, 410 (1981).

[25] Y. Yuan and Y. Iwasawa, J. Phys. Chem. B **106**, 4441 (2002).

[26] S. Ling, D. Mei, and M. Gutowski, Catal. Today **165**, 41 (2011).

[27] K. Biswas, S. V. Bhat, and C. N. R. Rao, J. Phys. Chem. C **111**, 5689 (2007).

[28] K. Biswas *et al.*, J. Phys.: Condens. Matter **19**, 436214 (2007).

[29] J.-E. Jorgensen, J. Staun Olsen, and L. Gerward, J. Appl. Cryst. **33**, 279 (2000).

[30] B. Houser and R. Ingalls, Phys. Rev. B **61**, 6515 (2000).

[31] E. Suzuki, Y. Kobayashi, S. Endo, and T. Kikegawa, J. Phys.: Condens. Matter **14**, 10589 (2002).

[32] J. E. Schirber *et al.*, Phys. Rev. B **29**, 4150 (1984).

[33] T. Chatterji and G. McIntyre, Solid State Commun. **139**, 12 (2006).

[34] M. Tsukada, N. Tsuda, and F. Minami, J. Phys. Soc. Jpn. **49**, 1115 (1980).

[35] D. Vanderbilt, Phys. Rev. B **41**, 7892 (1990).

[36] D. R. Hamann, M. Schlüter, and C. Chiang, Phys. Rev. Lett. **43**, 1494 (1979).

[37] P. Giannozzi *et al.*, J. Phys.: Condens. Matter **21**, 395502 (2009).

[38] J. P. Perdew and A. Zunger, Phys. Rev. B **23**, 5048 (1981).

[39] J. E. Schirber and B. Morosin, Phys. Rev. Lett. **42**, 1485 (1979).

[40] Y. X. Wang, M. Arai, T. Sasaki, and C. L. Wang, Phys. Rev. B **73**, 035411 (2006).

[41] C. Cheng, K. Kunc, and M. H. Lee, Phys. Rev. B **62**, 10409 (2000).

[42] J. Padilla and D. Vanderbilt, Phys. Rev. B **56**, 1625 (1997).

[43] E. Heifets *et al.*, Surf. Sci. **513**, 211 (2002).

[44] N. Li *et al.*, J. Appl. Phys. **107**, 123704 (2010).

[45] F. Cora, M. G. Stachiotti, C. R. A. Catlow, and C. O. Rodriguez, J. Phys. Chem. B **101**, 3945 (1997).

[46] M. G. Stachiotti, F. Cora, C. R. A. Catlow, and C. O. Rodriguez, Phys. Rev. B **55**, 7508 (1997).

[47] K. Biswas and C. N. R. Rao, J. Phys. Chem. B **110**, 842 (2006).

[48] Y. Luo, A. Aubry, and J. B. Pendry, Phys. Rev. B **83**, 155422 (2011).

[49] H. Xu, J. Aizpurua, M. Käll, and P. Apell, Phys. Rev. E **62**, 4318 (2000).

[50] J. P. Camden *et al.*, Journal of the American Chemical Society **130**, 12616 (2008).

[51] P. L. Stiles, J. A. Dieringer, N. C. Shah, and R. P. V. Duyne, Annual Review Analytical Chemistry **1**, 601 (2008).

[52] S. M. Morton, E. Ewusi-Annan, and L. Jensen, Phys. Chem. Chem. Phys. **11**, 7424 (2009).

[53] L. Tong, T. Zhu, and Z. Liu, Chem. Soc. Rev. **40**, 1296 (2011).

[54] Z.-Q. Tian, B. Ren, and D.-Y. Wu, The Journal of Physical Chemistry B **106**, 9463 (2002).

[55] S. Nie and S. R. Emory, Science **275**, 1102 (1997).

[56] J. Jiang, K. Bosnick, M. Maillard, and L. Brus, J. Phys. Chem. B **107**, 9964 .

[57] K. Tonigold and A. Gro, The Journal of Chemical Physics **132**, (2010).